World Electric Vehicle Journal

Article

A Physical-Based Vibro-Acoustic Numerical Model of a Permanent Magnet Synchronous Motor

Dario Barri, Federico Soresini, Giacomo Guidotti, Pietro Agostinacchio, Federico Maria Ballo and Massimiliano Gobbi *

Department of Mechanical Engineering, Politecnico di Milano, Via Privata Giuseppe La Masa, 20156 Milan, Italy
* Correspondence: massimiliano.gobbi@polimi.it

Abstract

With the growing demand for hybrid and electric vehicles, the accurate prediction of NVH (Noise, Vibration, and Harshness) behavior in Permanent Magnet Synchronous Machines (PMSMs) has become a critical aspect of electric motor design. This paper presents a detailed modeling approach for electromagnetic-induced noise and vibrations in PMSMs, integrating both analytical and numerical methods. The model focuses on quantifying the contributions of radial and tangential electromagnetic forces, which are key drivers of vibro-acoustic responses. The analytical part employs curved beam theory and a simplified acoustic model, offering rapid insights during early design stages. In parallel, a detailed numerical model based on finite element analysis is developed using a physics-based approach that accounts for the actual geometry and material properties of the PMSM prototype. This allows for enhanced accuracy without relying on experimental material parameter identification. Moreover, the detailed model includes the fluid–structure interaction introduced by the channels of the cooling fluid of the electric machine, which, although poorly addressed by the existing literature, was found to play a key role in driving the vibrational behaviour of the structure. By combining analytical speed with numerical precision, the proposed approach enables consistent and physically-based NVH predictions across various design phases, ultimately supporting improved electric machine performance and reducing development time and costs. Validation against experimental data confirms the ability of the model to accurately predict both sound pressure levels and housing surface vibrations. The novelty of this work lies in its integration of fluid–structure interaction and material modeling without the need for empirical parameter tuning, offering a robust tool for NVH design in electric vehicle applications.

Keywords: electric motor; PMSM; preliminary design; analytical model; numerical model; noise prediction; physical modelling

Academic Editor: Aymeric Rousseau

Received: 13 March 2026
Revised: 9 April 2026
Accepted: 14 April 2026
Published: 18 April 2026

1. Introduction

Permanent Magnet Synchronous Motors (PMSMs) are widely used in the automotive industry, and, due to the global trend toward vehicle electrification, their design and production have become increasingly important. As electric motors replace internal combustion engines (ICEs) [1], they have emerged as a primary noise source in vehicles. Notably, their distinctive high-pitched noise can be particularly uncomfortable for passengers [2], making Noise, Vibration, and Harshness (NVH) analysis essential in modern vehicle design. As a result, the literature includes several reviews addressing the NVH behavior of electric machines [3–5].

https://doi.org/10.3390/wevj17040216

The first step in NVH analysis involves identifying the dominant noise sources. In PMSMs, the most significant contributors include structure-borne noise (e.g., from bearings and fasteners), aerodynamic noise (e.g., from fans and ducts of the cooling) and electromagnetic noise, which results from vibrations induced by electromagnetic forces acting on the stator teeth [6]. Among these, electromagnetic noise is typically the most prominent [5]. For this reason, the initial focus of NVH analysis is often on the calculation of electromagnetic forces. The subsequent steps involve the development of structural and acoustic models.

The electromagnetic forces acting on the stator teeth are generated within the air gap as a result of the interaction between the permanent magnet field and the armature field. In the literature, two methods are commonly used to calculate these electromagnetic forces for NVH analysis: the Maxwell Stress Tensor [7] and the Virtual Work Principle (VWP) [8]. Both radial and tangential forces act on the stator, with tangential forces becoming particularly significant under loaded motor conditions, as they are closely related to torque generation. The electromagnetic forces in PMSMs contain harmonic components in both time and space, which act as excitation sources for the stator. Resonance phenomena occur when the spatial order of a harmonic excitation aligns with a structural mode shape and its frequency matches the natural frequency of the structure, leading to pronounced vibration amplitudes and increased acoustic noise. These vibrations are perceived as detrimental tonal components inside the vehicle cabin [9]. This underscores the importance of thoroughly analyzing the harmonic spectrum of electromagnetic forces under various operating conditions.

Electromagnetic excitations can also be categorized into two main types: rotating forces, which present a spatially lobed shape and travel around the air gap synchronously with the rotor, and pulsating forces, which oscillate at fixed positions relative to the stator (breathing modes). Each type influences the dynamic response of the motor differently [10]. The excitation of low-order lobed modes [11,12] and breathing modes [13,14] has been identified in the literature as a key contributor to vibration generation. In a PMSM, the minimum spatial order, denoted r_{min}, is determined by the greatest common divisor (GCD) of the stator slot number and rotor pole number. As a result, designers often face a trade-off between reducing r_{min} and mitigating the impact of breathing modes, since vibrational amplitudes tend to decrease as the mode order increases [15]. Optimizing slot and pole combinations at the design stage can increase the GCD, thereby reducing the presence of harmful harmonics and enhancing the machine's vibrational performance [16].

For the accurate prediction of vibrations and radiated noise, a detailed structural model of all components is essential. Analytical models typically focus on the stator, which is the component mostly affected by electromagnetic forces [7,17]. Common representations include cylindrical shell models or curved beam formulations [18–20]. Even in numerical studies, many works focus solely on stator deformations [12,21], neglecting the modeling of other critical components, such as the housing, rotor and cooling fluid. However, numerical models can capture all these components in detail, albeit at a higher computational cost.

Once the structural response is calculated, acoustic modeling completes the NVH simulation chain by converting vibration data into sound pressure predictions, enabling evaluation of the motor's acoustic emissions. Acoustic modeling has also been approached analytically. For instance, Ref. [7] explored acoustic emissions from simplified sources such as planar and curved radiators. When applied to PMSMs, infinitely long radiating cylinders have shown the highest accuracy. Among numerical methods, the finite element method (FEM), the boundary element method (BEM) and statistical energy analysis (SEA) are the most commonly used [5]. SEA is efficient for mid-to-high frequency ranges but suffers from reduced accuracy due to uncertainties and its dependency on subsystem division [5,7]. FEM is highly accurate, especially for near-field and internal cavity problems, but is computationally demanding due to full-domain meshing requirements [7,21]. BEM, which requires meshing only the boundaries, is more efficient for far-field acoustic analysis but is less suitable for near-field scenarios [7,22]. Thus, the choice of acoustic modeling method depends on the specific application and analysis requirements. The integration of electromagnetic, structural, and acoustic models is essential to achieve a comprehensive and predictive NVH simulation framework for PMSMs.

One of the key bottlenecks in achieving predictive model accuracy is the characterization of material parameters, particularly for laminated stator cores and winding assemblies. These components exhibit complex anisotropic behavior due to their layered and composite structure. This makes it challenging to directly define their mechanical properties. To address this, homogenization techniques [23] or experimental modal analyses are typically employed to estimate equivalent orthotropic properties [24–26]. Ciceo et al. [27] assume orthotropic behavior for the stator model and update the FEM material properties to match the results of experimental modal analysis. Although experimental approaches allow for the development of accurate models, they often depend on prototype-based testing. This limits the feasibility of fully predictive NVH simulations during early design stages and delays optimization until physical components become available. These methods commonly include sensitivity analyses of modal frequencies with respect to key material parameters (e.g., evaluating how natural frequencies vary with changes in shear moduli), helping to identify the most critical parameters to be tuned for accurate predictions [28]. To overcome the dependency on experimental testing, recent studies have explored alternative approaches to estimate equivalent parameters purely from theoretical or numerical models, aiming to enable predictive modeling already in the early stages of design. Yin et al. [29] proposed an experimental identification process for the material parameters of the stator and windings, based on an orthotropic modeling approach and starting from an initial guess derived from equivalent homogenized properties. In a subsequent work [20], the stator was modeled as anisotropic, and the authors proposed two different orthotropic modeling approaches for the windings: in the first, the windings are represented as columnar bodies, while in the second, they are modeled as thin-walled tubular bodies, which increase the equivalent mass and stiffness of the stator core. Sun et al. [30] evaluate the anisotropic material parameters by modeling the stator core as a periodic repetition of a cubic unit cell. By applying tensile and pure shear loads in various directions, they compute the corresponding stress and strain responses. The application of appropriate periodic boundary conditions to the unit cell is crucial for accurately determining the effective material properties. This approach is also extended to the winding and impregnation varnish. The resulting maximum error in natural frequency predictions is within 2.1%. Saki et al. [31] proposed a semi-analytical FEM-based approach to evaluate key force harmonics and influential components of the stator system, validating their findings against experimental results. To simplify the complex multi-material teeth-winding region, they introduced two equivalent models. The first model employs an equivalent FEM-based representation of the slot materials, while the second uses an equivalent shell, evaluated through a combination of finite element and analytical methods.

Other works that analyze a complete NVH framework for electric motors can be found in the literature. Yongchao et al. [32] performed an NVH analysis at the electromagnetic level to optimize the rotor slotting effect. No structural or acoustic models were defined; instead, the electromagnetic results were directly validated through experimental tests conducted in a semi-anechoic chamber. Song et al. [33] present a complete numerical procedure for the NVH analysis of Permanent Magnet Synchronous Motors (PMSMs) in automotive applications, which can be employed to assess electric vehicle performance. The study neglects the contribution of tangential forces and attributes the maximum vibration deformation to the excitation of the zero-th structural mode. A complete multiphysics approach was also presented in [34], highlighting the importance of considering eccentricity effects. In this study, lumped forces on each stator tooth were used to evaluate the acoustic emissions, without performing any experimental validation. Recently, hybrid modeling approaches have gained attention as a means to accelerate NVH predictions. For example, Zhao et al. [35] combined subdomain modeling with a structural finite element model to predict vibrations in different Surface-Mounted PMSM topologies.

However, the previously cited works overlook the NVH impact of the cooling system, which is essential for thermal management in high-performance motors. The fluid medium, typically a water–glycol mixture circulating through a water jacket, introduces fluid–structure interactions that can significantly alter the system's dynamic response. To date, only a few studies have addressed this phenomenon [36,37], with [36] presenting a numerical NVH modeling approach for a simplified cooling system in PMSMs. No existing studies in the literature present a complete NVH model of a real-world automotive electric motor that also includes the cooling system.

Contribution

The objective of this work is to develop a predictive NVH model for a PMSM, intended to support the entire design process from early concept to final validation.

The main contributions of this study are as follows:

- The development of a predictive model capable of evaluating the NVH behavior without the need for a physical prototype. This is achieved through a physics-based modeling approach, where the material properties are defined using the known isotropic characteristics of the components, rather than relying on experimental identification, as is common in conventional models in the literature. This approach offers a significant advantage, as it eliminates the need for early-stage physical testing to extract mechanical properties, which would otherwise require a prototype to be available for experimental correlation.
- The novel investigation of the cooling fluid effects on NVH performance: this work proposes a complete NVH model of a real-world PMSM, featuring a detailed representation of the spiral water jacket to account for fluid–structure interactions, with no simplifications applied to the cooling system representation.

The paper is structured as follows: Section 2 introduces the NVH modeling framework, presenting the PMSM under analysis and evaluating the electromagnetic forces under the considered operating conditions. In Section 3, the noise emissions of the electric motor are assessed using an analytical model based on curved beam theory, considering both drag and on-load scenarios. Section 4 presents the FE structural model of the PMSM, developed using a physics-based approach with particular attention to the definition of equivalent material properties and the modeling of the coolant fluid. Section 5 details the experimental validation of the FEM model, first through the comparison of experimental and numerical mode shapes and frequency response functions (FRFs), and subsequently by validating the simulated vibration response of the motor's external surface using accelerometer measurements. Finally, Section 6 describes the acoustic domain modeling and presents a comparison between numerical and experimental sound pressure levels. The conclusions are summarized in the final section.

2. NVH Modelling

The motor under study is a 6–36 pole–slot combination Permanent Magnet Synchronous Motor (PMSM) with distributed hairpin winding, developed for traction applications in the automotive sector, able to deliver a peak power of 130 kW with a rated speed of 25 kRPM. As outlined previously, the modeling process is divided into three stages: electromagnetic, structural and acoustic, as illustrated in Figure 1. The result of each stage is used as input for the next one, ensuring a consistent and physics-driven workflow across domains. Particular attention is devoted to the numerical model, which is validated through a two-step correlation procedure. The first step involves a simplified submodel, referred to as the Jacket model, comprising only the stator, rotor, jacket, and resin. This configuration isolates the core vibrational modes before incorporating the housing and fluid. The second step extends the validation to the complete PMSM system. Finally, the NVH simulation results are compared with experimental data provided by the manufacturer, confirming the validity and reliability of the proposed approach. Validation has been performed under multiple load and speed conditions, ensuring the reliability of the model across a representative range of operating scenarios.

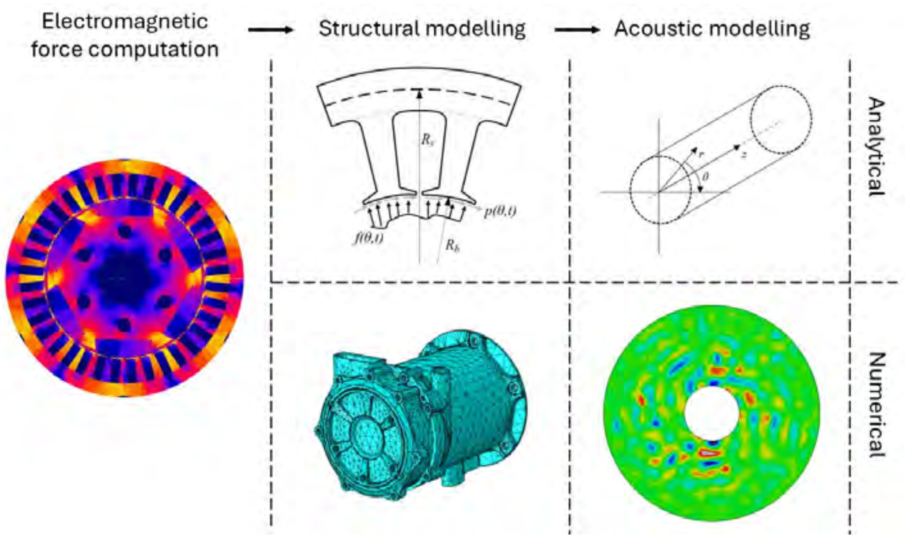

Figure 1. NVH modeling approaches.

Electromagnetic Force Computation

In this section, the electromagnetic forces, computed using a numerical approach, specifically a 2D finite element method, are presented, as they serve as the input for both the analytical and numerical NVH models. The cross-sectional geometry of the machine is shown in Figure 2. The electromagnetic forces in the air gap are calculated in both radial and tangential directions using the Maxwell Stress Tensor. These quantities represent surface pressures (i.e., force per unit area) acting on the stator teeth due to the magnetic field distribution. The components of the magnetic flux density, and consequently the resulting Maxwell pressures, vary both spatially along the air gap (as a function of the angular coordinate α) and temporally (as a function of time t) [15]. Accurately capturing this spatial–temporal dependence is essential to identify the harmonic content of the excitation and its potential interaction with structural resonances. The expressions for the radial and tangential components of the Maxwell pressure in cylindrical coordinates are given by

$$\begin{cases} P_r(\alpha,t) = \frac{1}{\mu_0}\left(B_r^2(\alpha,t) - B_t^2(\alpha,t)\right) \\ P_t(\alpha,t) = \frac{1}{\mu_0}B_r(\alpha,t)B_t(\alpha,t) \end{cases} \quad (1)$$

where $P_r(\alpha, t)$ and $P_t(\alpha, t)$ are the radial and tangential components of the Maxwell pressure, $B_r(\alpha, t)$ and $B_t(\alpha, t)$ are the respective components of the magnetic flux density in the air gap, and μ_0 is the permeability of free space.

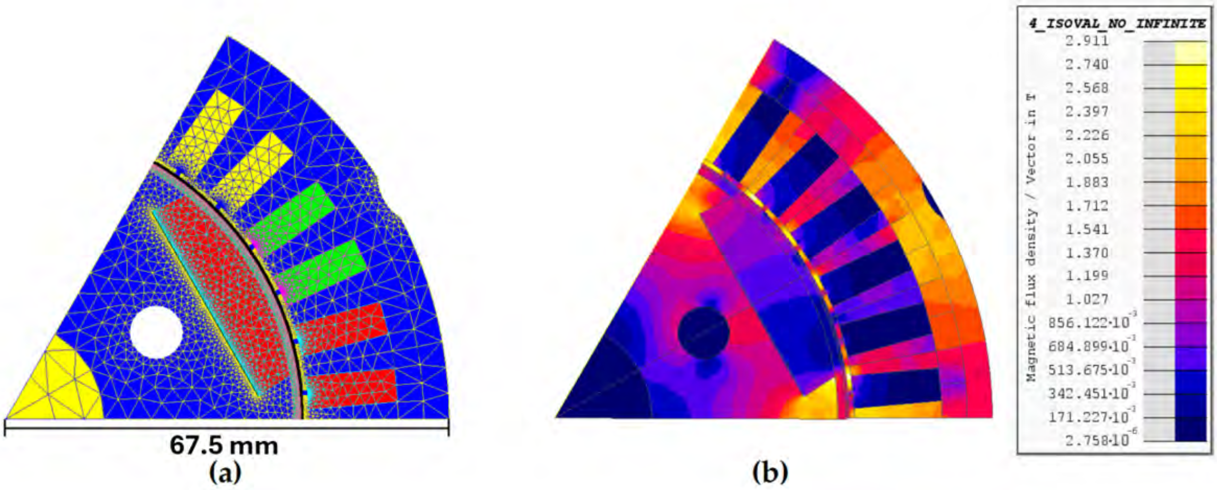

Figure 2. Section view: FEM model with mesh (**a**) and magnetic field distribution (**b**).

For the computation of the electromagnetic excitations, a numerical electromagnetic model based on first-order finite elements was employed. In the model, the stator and rotor laminations are made of NO20 while the magnets are composed of VACODYM 983 TP.

Two key parameters were considered to ensure the accurate characterization of the electromagnetic forces: the number of time steps used in the transient simulation and the number of nodes used to compute the forces on the stator teeth surface. These parameters are critical to capture the temporal and spatial evolution of the force distribution with sufficient resolution. In particular, a mesh sensitivity analysis was carried out on the number of nodes along the tooth head surface, where the electromagnetic forces are computed. Two meshing alternatives were evaluated, differing in the number of elements across the tooth width: 10 and 20 elements. In both cases, the mesh was symmetrically distributed to include a central node, allowing for the correct application of force components along the tooth centerline. To assess the effect of mesh density, the radial force time histories at each tooth were extracted and subjected to one-dimensional Fast Fourier Transform. The resulting spectra revealed negligible differences between the two configurations, as reported in Table 1, confirming that ten elements are sufficient for accurately capturing the electromagnetic excitation. Based on this result, the coarser mesh with ten elements was selected to reduce computational cost without compromising accuracy. Additionally, two motor operating conditions were simulated. The first one is the drag condition, in which the motor is unpowered and mechanically driven by the test bench. The second one is the full-load condition, in which the motor is maintaining a constant maximum torque in the range 0–10,000 rpm. This last operating condition was simulated by imposing the rated maximum current values, corresponding to $I_d = -253$ Arms and $I_q = 297$ Arms. The radial forces and the corresponding 2D spectra, in both the drag and full-load conditions, are shown in Figure 3. It can be observed that, under full-load conditions, even the lower-amplitude harmonics increase significantly.

Table 1. Mesh sensitivity analysis on the spectrum of tooth resultant radial force.

Time Orders	Radial Force (10 Elements) [N]	Radial Force (20 Elements) [N]	Relative Error [%]
0	99.28	99.50	−0.22
6	92.80	95.95	−3.29
12	19.88	19.96	−0.40
18	5.87	5.87	0.06
24	5.98	5.99	−0.17
30	1.07	1.08	−0.93

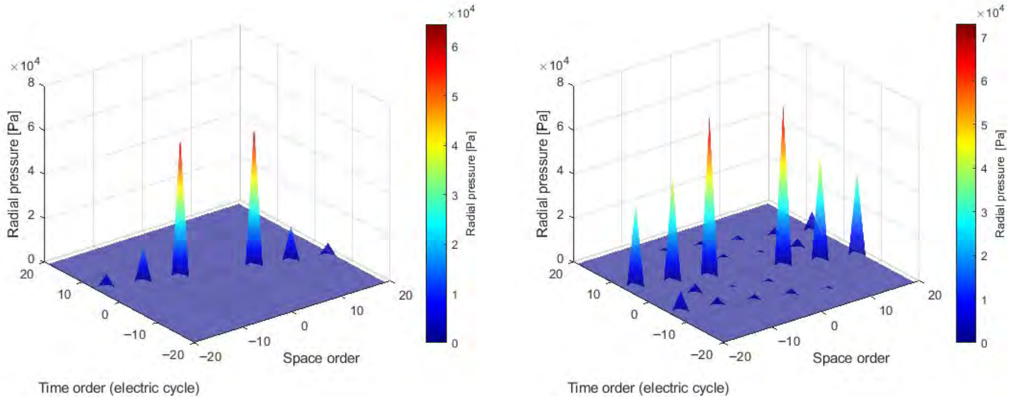

(**a**) (**b**)

Figure 3. Radial forces in the frequency domain in the drag condition (**a**) and full-load condition (**b**). The main peaks are at (−2,6) and (6,−2) space-time orders.

From the analysis of the spectra (Table 2), it can be observed that the main component is (6,6), while the dominant contribution of the breathing mode occurs at the multiples of LCM (poles, slots) [10], which in this application corresponds to the 36th order. By comparing the drag and full-load conditions, it is noted that the largest increase occurs at the (0,36) component rather than at (6,6). It should be noted that, unlike the temporal orders mentioned so far, the time orders in the spectrogram refer to the electrical frequency and not the the mechanical one. The mechanical order n_m and the electrical order n_e are related by the expression $n_m = n_e \cdot \frac{P}{2}$, where P is the number of poles. Understanding this correspondence is essential for correctly interpreting the spectrograms and identifying which harmonics are of electrical origin.

Table 2. Comparison of harmonic amplitude between the drag and full-load conditions.

Harmonic Order (Space,Time)	Drag Amplitude [Pa]	Full-Load Amplitude [Pa]
(0,36)	94.7	3066.4
(6,6)	64,480	73,038

3. Analytical Model

The developed analytical model is based on the one derived by Ballo et al. [38] and models the PMSM as a curved beam with equivalent material parameters that are determined considering the stator yoke, teeth, windings and housing. The model takes as the input the harmonics of the radial and tangential forces developed in the air gap. However, the curved beam theory requires the load to be applied on the neutral axis, in addition to the previous terms an additional distributed bending moment is introduced , to account for the lever arm effect of the tooth body. A representation of the equivalent structure and applied load is shown in Figure 4.

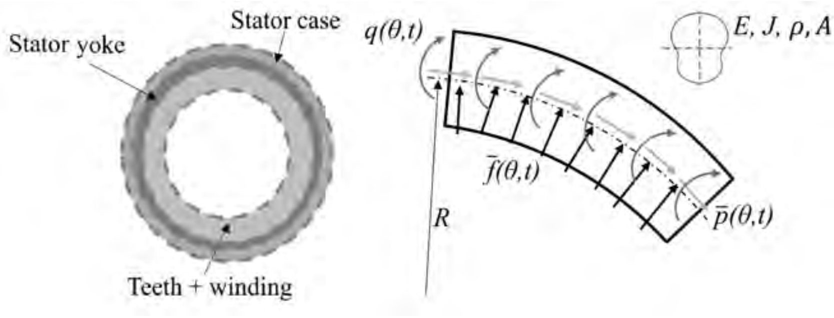

Figure 4. Scheme of the equivalent stator cylindrical structure and force applied to the curved beam.

The equation of motion is constructed by imposing the equilibrium condition in the three directions and by assuming small displacements and the conservation of the total length of the beam

$$\frac{\partial^6 u}{\partial\theta^6} + 2\frac{\partial^4 u}{\partial\theta^4} + \frac{\partial^2 u}{\partial\theta^2} - \frac{R^4}{EJ}\left(\frac{\partial\bar{p}}{\partial\theta} + \frac{\partial^2\bar{f}}{\partial\theta^2} + \frac{1}{R}\frac{\partial^3 q}{\partial\theta^3} + \frac{1}{R}\frac{\partial q}{\partial\theta}\right) = \frac{\rho A R^4}{EJ}\frac{\partial^2}{\partial t^2}\left(u - \frac{\partial^2 u}{\partial\theta^2}\right) \quad (2)$$

where u is the radial displacement of the beam at the neutral axis, R is the radius of the equivalent curved beam, and σ_r and σ_t represent the radial and tangential components of the electromagnetic force density, respectively. The term m denotes the transport moment, while EJ is the equivalent bending stiffness, computed from the bending stiffness of the three annular regions. A is the cross-sectional area, t is time, and θ is the spatial coordinate along the arc of the beam [38,39].

The natural frequencies of the system can be estimated from the Equation (2) by setting the loading terms ($\bar{f}$, $\bar{p}$, and q) to zero and assuming a harmonic solution $u(\theta, t) = U \cdot e^{i(n\theta+\omega_n t)}$. Under these assumptions and considering free boundary conditions, the natural frequencies of the system ω_n can be obtained by solving the characteristic equation, which is

$$\omega_n{}^2 = \frac{EJ}{\rho A R^4} \cdot \frac{n^6 - 2n^4 + n^2}{n^2 + 1} \qquad n = 2, 3, 4, \ldots \quad (3)$$

The steady-state overall response of the structure can be expressed as the superposition of the harmonic components of the radial displacement, denoted by $Y^r_{n,k}$ and $Y^\tau_{n,k}$, which represent the displacement response to radial and tangential electromagnetic excitations, respectively. Here, n and k indicate the spatial and temporal harmonic orders.

$$Y^r_{n,k} = \frac{F_{n,k}}{\rho A \omega_n^2}\frac{R_b}{R}\frac{n^2}{n^2+1}\eta_{n,k} \quad (4)$$

$$Y^\tau_{n,k} = -\frac{P_{n,k}\, i}{\rho A \omega_n^2}\frac{R_b}{R}\frac{n}{n^2+1}\left[1 + h(n^2-1)\right]\eta_{n,k} \quad (5)$$

where $h = \frac{R-R_b}{R}$, ρ is the equivalent density of the curved beam, $F_{n,k}$ and $P_{n,k}$ are respectively the harmonics of the radial and tangential forces, ω_n is the natural frequency of the n-th mode, R is the radius of the neutral axis, R_b is the bore radius, A is the cross-sectional area of the equivalent beam, and $\eta_{n,k}$ is the modal amplification factor [38,39].

Once the radial displacement field is computed, the acoustic emission of the motor can be estimated. The acoustic model is based on that of an infinitely long cylindrical radiator [7]. Assuming uniform radial displacement along the axial direction, the resulting acoustic pressure field can be derived as follows

$$s(r;\theta;t) = \sum_{k,n=-\infty}^{+\infty} -\frac{iV_{n,k}\rho_0 c_0}{k_0 \frac{dH_n^{(2)}(k_0 R_{out})}{d(k_0 R_{out})}} H_n^{(2)}(k_0 r) e^{i(n\theta + k\omega_0 t)} \tag{6}$$

where $V_{n,k}$ are the harmonic amplitudes of the radial velocity of the surface, which are obtained by time derivative of the radial displacement u, $H_n^{(2)}$ is the second kind Hankel function of order n, k_0 is the acoustic wave number and it is calculated as $\frac{k \cdot \omega_0}{c_0}$, ρ_0 is the air density, c_0 is the speed of sound in the air, R_{out} is the outer radius of the cylindrical surface, and r is the radial coordinate.

Then, an A-weighting filter is applied to the sound pressure to account for human sensitivity, as the audible frequency band for the human ear ranges form 20 Hz to 20,000 Hz [7]. The results of this procedure under drag conditions are shown in the spectrogram in Figure 5a in terms of the sound pressure level (SPL) [7]. Two main peaks can be observed in the spectrum. The first occurs at the sixth order, in accordance with the findings of the electromagnetic forces and mainly caused by the excitation of mode 2. The second peak appears at the 36th order and is attributed to the excitation of the breathing mode. This is consistent with the motor's architecture, as pulsating force harmonics typically occur at integer multiples of the least common multiple (LCM) between the number of poles and slots [16]. Following this rule, the next significant excitation occurs at the 72nd order. This is confirmed in the SPL map by a secondary yellow peak located just below the dominant red peak, corresponding to the 72nd time order.

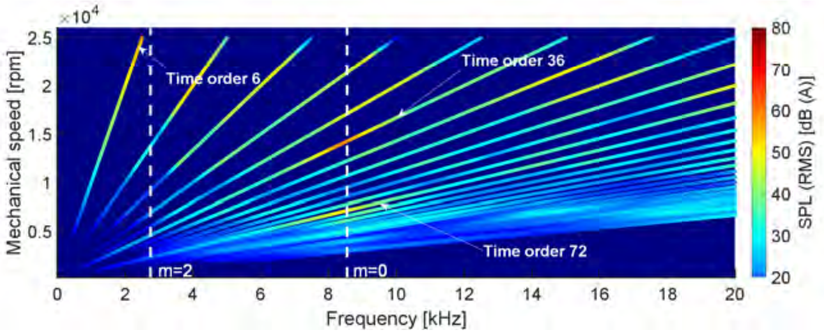

(**a**)

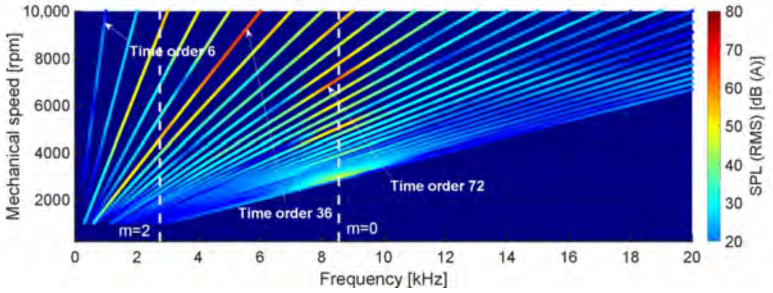

(**b**)

Figure 5. Analytical SPL spectrograms. (**a**) Drag condition. (**b**) Full-load condition.

In Figure 5b, the spectrogram of the acoustic pressure under full-load conditions is shown. The results are consistent with those obtained under drag conditions. However, a higher overall amplitude in terms of SPL is observed, due to the increased harmonic content of the electromagnetic excitations in full-load operation. Note that the full-load test was performed under constant torque conditions—therefore, up to 10,000 rpm.

4. Numerical Structural Model

The numerical model incorporates the complete set of components involved in the test bench setup, making it significantly more complex than most models found in the literature [20,27,29,30], which typically focus primarily on the stator. Figure 6 shows the exploded view of all the components included in the FEM model.

The flange, jacket, plate, and housing are made of aluminum. As far as the stator, rotor and windings are concerned, the structural model is built following a physics-based approach, where material properties are derived from the isotropic properties of the constituent materials, avoiding the need for experimental testing. Details about the modeling approach selected for these components are given in the following sections. Particular care is also taken in modeling the coolant fluid, whose properties in the numerical model are described in Section 4.3.

The base materials accounted in the FEM models and used in the next homogenization approach are listed in Table 3. The values of the material parameters are compatible with the ones used in other publications [36,40].

Table 3. Material data sheet used as input for homogenization. CFRP refers to Carbon Fiber-Reinforced Polymer.

Material	Density [kg/m^3]	Young Modulus [GPa]	Poisson's Ratio [-]
Steel (Rotor)	7800	210	0.30
CFRP (Banding)	1570	225	0.29
Resin	2050	10 (E_{resin})	0.35 (ν_{resin})
Copper (Windings)	8960	115 (E_{copper})	0.33 (ν_{copper})
NdFeB (Magnets)	7700	140	0.24
Polymer (Connections)	1650	14.7	0.35
Varnish (Stator lamination)	2100	1 ($E_{varnish}$)	0.35 ($\nu_{varnish}$)
Silicon steel (Stator lamination)	7650	185 (E_{steel})	0.30 (ν_{steel})

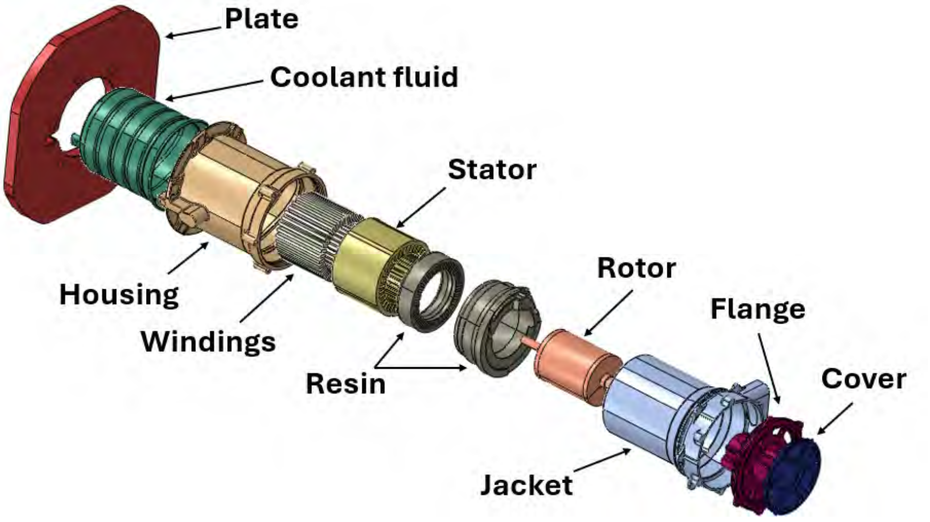

Figure 6. Exploded view of the FEM model.

4.1. Rotor Sub-Assembly

The rotor sub-assembly includes the steel shaft, balancing discs, magnet support, neodymium magnets and CFRP banding. Although it maintains the same external geometry, as can be seen in Figure 7, it is internally divided into five sections with different densities. These are computed by averaging the densities ρ_i of the constituent materials, weighted by their volume fractions ξ_i, as shown in Equation (7):

$$\rho_{\text{section}} = \sum_i \rho_i \xi_i \tag{7}$$

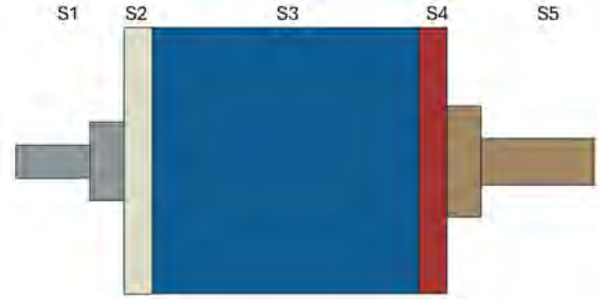

Figure 7. Rotor sections.

This approach preserves the original axial mass distribution. The rotor assembly is very stiff, as it is designed to keep flexural natural frequencies outside the operating range of the motor. For this reason, this assembly has been modeled as a rigid solid supported by springs representing the bearings.

4.2. Laminated Stator, Winding and Resin

The stator lamination stack and the windings are heterogeneous materials, composed of steel and varnish, and of copper and resin, respectively. As shown in Figure 8, these are modeled as transversely isotropic materials obtained using homogenization techniques based on the Voigt (parallel) and Reuss (series) rules [17]. The base materials used for the homogenization process are listed in Table 3. These isotropic properties serve as the input for the Voigt and Reuss homogenization formulas described in the following sections.

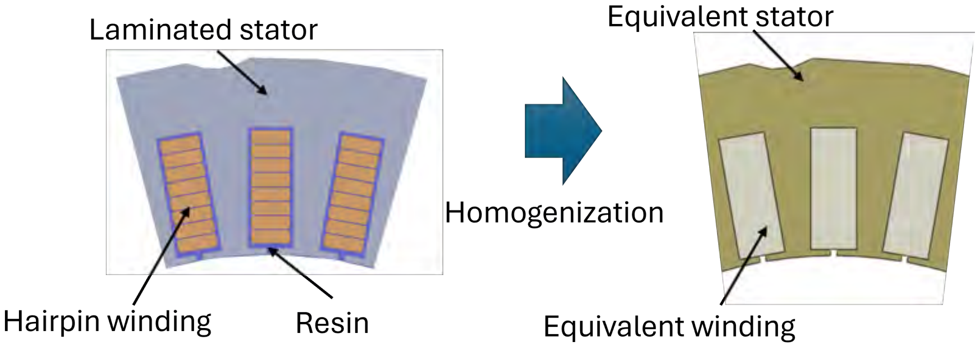

Figure 8. Homogenization approach for stator, winding, and resin.

As far as winding modeling is concerned, in this case, because of the presence of hairpin windings, it becomes necessary to introduce some corrective coefficients to accurately represent the properties of the windings. These correction coefficients have been obtained by means of the ANSYS Material Designer (Ansys 2024 R1) [41], following the approach described in [30]. For motors without hairpin windings, the results of the analytical formulas are more aligned with those of the ANSYS Material Designer; therefore, in such cases, the corrective coefficients can be neglected.

In the following formulas, the subscripts r, θ and x indicate respectively the radial, tangential and axial directions.

4.2.1. Voigt Rule (Parallel Phases)

When strain is consistent across phases, the Voigt rule applies. The effective material properties are as follows:

Stator (radial and tangential directions):

$$\begin{aligned}
E_{r,stator} = E_{\theta,stator} &= E_{steel}\xi_{steel} + E_{varnish}\xi_{varnish} \\
G_{r\theta,stator} &= G_{steel}\xi_{steel} + G_{varnish}\xi_{varnish} \\
\nu_{r\theta,stator} &= \frac{E_{r,stator}}{2G_{r\theta,stator}} - 1
\end{aligned}$$

where E_{steel} and $E_{varnish}$ represent the elastic moduli of silicon steel and varnish, listed in Table 3, while ξ_{steel} (96%) and $\xi_{varnish}$ (4%) denote the corresponding volume fractions relative to the total stator volume, and G_{steel} and $G_{varnish}$ are the shear moduli of the respective materials.

Windings (axial direction):

$$\begin{aligned}
E_{x,windings} &= E_{resin}\xi_{resin} + E_{copper}\xi_{copper} \\
G_{\theta x,windings} = G_{rx,windings} &= k_1(G_{resin}\xi_{resin} + G_{copper}\xi_{copper}) \\
\nu_{\theta x,windings} = \nu_{rx,windings} &= k_2\left(\frac{E_{x,\text{windings}}}{2G_{\theta x,\text{windings}}} - 1\right)
\end{aligned}$$

where E_{resin} and E_{copper} represent the elastic moduli of resin and copper, reported in Table 3, while ξ_{resin} (41%) and ξ_{copper} (59%) denote their corresponding volume fractions relative to the homogenized windings volume, G_{resin} and G_{copper} are the shear moduli of the respective materials, and k_1 and k_2 are the corrective coefficients obtained from the ANSYS Material Designer.

4.2.2. Reuss Rule (Series Phases)

When stress is the same in all phases, the Reuss rule is used:

Stator (axial direction):

$$\begin{aligned}
E_{x,stator} &= \frac{E_{steel}E_{varnish}}{\xi_{steel}E_{varnish} + \xi_{varnish}E_{steel}} \\
\nu_{\theta x,stator} = \nu_{rx,stator} &= \frac{\nu_{steel}\nu_{varnish}}{\xi_{steel}\nu_{varnish} + \xi_{varnish}\nu_{steel}}
\end{aligned}$$

Windings (radial and tangential directions):

$$\begin{aligned}
E_{r,windings} = E_{\theta,windings} &= k_3\frac{E_{resin}E_{copper}}{\xi_{resin}E_{copper} + \xi_{copper}E_{resin}} \\
\nu_{r\theta,windings} &= k_4\frac{\nu_{resin}\nu_{copper}}{\xi_{resin}\nu_{copper} + \xi_{copper}\nu_{resin}}
\end{aligned}$$

where k_3 and k_4 are corrective coefficients obtained from ANSYS Material Designer.

4.2.3. Mixed-Plane Shear Modulus

To address complex stress conditions involving both parallel and series behaviors, an equivalent Young's modulus is used as proposed by Chai et al. [17]. This allows for the calculation of the mixed-plane shear modulus.

Stator:

$$\begin{aligned}
q_{\text{stator}} &= \frac{\xi_{steel} E_{steel}}{2(1+\nu_{\text{steel}})} + \frac{\xi_{varnish} E_{varnish}}{2(1+\nu_{\text{varnish}})} \\
E_{\text{mix,stator}} &= \frac{\xi_{steel} E_{steel}(q_{\text{stator}} + E_{varnish}) + \xi_{varnish} E_{varnish}(q_{\text{stator}} + E_{steel})}{\xi_{steel}(q_{\text{stator}} + E_{varnish}) + \xi_{varnish}(q_{\text{stator}} + E_{steel})} \\
G_{rx,stator} &= G_{x\theta,stator} = \frac{E_{\text{mix,stator}}}{2(1+\nu_{rx,stator})}
\end{aligned}$$

where ν_{steel} and $\nu_{varnish}$ represent the Poisson's ratio of silicon steel and varnish, listed in Table 3.

Windings:

$$\begin{aligned}
q_{\text{windings}} &= \frac{\xi_{resin} E_{resin}}{2(1+\nu_{\text{resin}})} + \frac{\xi_{copper} E_{copper}}{2(1+\nu_{\text{copper}})} \\
E_{\text{mix,windings}} &= \frac{\xi_{copper} E_{copper}(q_{\text{windings}} + E_{copper}) + \xi_{resin} E_{resin}(q_{\text{windings}} + E_{resin})}{\xi_{resin}(q_{\text{windings}} + E_{copper}) + \xi_{copper}(q_{\text{windings}} + E_{resin})} \\
G_{rx,windings} &= k_5 \frac{E_{\text{mix,windings}}}{2(1+\nu_{rx,windings})}
\end{aligned}$$

where ν_{copper} and ν_{resin} represent Poisson's ratio of copper and resin, listed in Table 3, and k_5 is a corrective coefficient obtained from the ANSYS Material Designer.

The density of the homogenized materials are obtained using Equation (7) and the values listed in Table 3.

The mechanical properties obtained through this procedure are summarized in Table 4 and are consistent with those reported in [30].

Table 4. Mechanical properties of homogenized stator and winding materials.

Parameter	Stator	Windings
Density [kg/m^3]	7428	6020
E_r [GPa]	177.64	4.04
E_θ [GPa]	177.64	4.04
E_x [GPa]	22.13	50.8
ν_{rx} [–]	0.301	0.08
$\nu_{r\theta}$ [–]	0.3	0.41
$\nu_{\theta x}$ [–]	0.301	0.08
G_{rx} [GPa]	61.72	0.32
$G_{r\theta}$ [GPa]	68.32	1.43
$G_{x\theta}$ [GPa]	61.72	0.32

A constant structural damping equal to 3% has been assigned to the stator lamination to account for dynamic viscous effects. This value is consistent with other similar case studies in the literature [36,42].

4.3. Coolant Fluid

Another significant component included in the model is the cooling fluid. This PMSM features a complex cooling jacket geometry with a spiral channel formed along the inner surface of the housing. A 50/50 mixture of water and glycol flows through these channels, situated between the jacket and the housing. The fluid is modeled as an acoustic domain using AC3D10 mesh elements, and its material properties are defined by density and bulk modulus, whose values are taken from [36] and are listed in Table 5.

By modeling it as an acoustic domain, a fluid–structure interaction is introduced, enhancing the FE formulation into a coupled dynamic problem.

Table 5. Material properties of the cooling fluid.

Material	Density [kg/m^3]	Bulk Modulus [GPa]
Cooling fluid	1100	3

Modeling this interaction numerically adds novelty to the work, as investigations on the impact of cooling fluids in PMSM NVH models are limited and, to the best of the authors' knowledge, have not been performed on real-world PMSMs. Only a study conducted by the authors on a simplified cooling topology highlights that its presence significantly alters the structural response by inducing additional eigenmodes [36]. Figure 9 shows the CAE model of the coolant fluid domain. The fluid mesh is connected to the housing and jacket surfaces through a tie interaction, which enforces identical displacements at the shared interface nodes, enabling fluid–structure coupling.

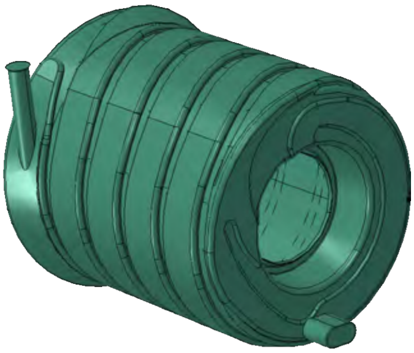

Figure 9. CAE modelling of the coolant fluid domain.

5. Experimental Validation

A comprehensive validation process has been developed for the numerical motor assembly. The procedure begins with a simplified configuration, referred to as the Jacket model, containing only the core elements: the stator, rotor, jacket, windings and resin. This setup enables the identification and correlation of the primary stator deformation modes responsible for vibration. Subsequently, the most complete configuration, referred to as the Complete model, is analyzed. It reproduces the NVH test conditions, with the motor mounted on the test bench, and includes the housing, cooling fluid and bench structure. Accurate modeling of this setup is essential for reliable NVH simulation.

The Jacket model, shown in Figure 10, is tested under free–free boundary conditions. Modal analysis and hammer tests were carried out to evaluate its dynamic behavior.

(**a**) (**b**) (**c**)

Figure 10. Jacket model. (**a**) Experimental setup. (**b**) Position of the accelerometers. (**c**) Numerical model.

https://doi.org/10.3390/wevj17040216

The accelerometers employed for this and all the other tests mentioned in this article are PCB piezoelectronics 339A30 Triaxial ICP® accelerometers by PCB Piezotronics, Inc. (Depew, NY, USA). Their characteristics are listed in Table 6.

The input excitation is provided by a PCB 086C03 impact hammer by PCB Piezotronics, Inc. (Depew, NY, USA). Its features are described in Table 7.

Table 6. Properties of the PCB piezoelectronics 339A30 Triaxial ICP® accelerometers.

Property	Value	Property	Value
Sensitivity	10 mV/g	Measurement range	±500 g pk
Frequency range	2–8000 Hz	Resonant frequency	≥25 kHz

Table 7. Properties of PCB 086C03 impact hammer.

Property	Value	Property	Value
Sensitivity	2.25 mV/N	Measurement range	±2224 N pk
Resonant frequency	≥22 kHz		

The experimental modal analysis (EMA) was performed using a roving accelerometers technique, with acceleration data acquired at 16 circumferential points on the jacket, across four axial sections of the motor. After a series of hammer tests, the frequency of the modes of the Jacket model have been estimated by means of the PolyMax method [43]. The frequency range was limited to 5000 Hz, due to coherence loss at higher frequencies. As shown in Table 8, the numerical model matches the experimental results well, with a small overestimation of natural frequencies (approximately 3.5%), indicating slightly higher modeled stiffness.

Table 8. Comparison between experimental and numerical natural frequencies f_n and mode shapes.

Mode	Exp. f_n	Experimental Mode Shape	Num. f_n	Numerical Mode Shape	err_{rel}
2,0	1975 Hz	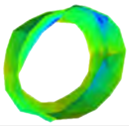	2044 Hz	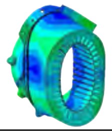	3.5%
2,1	2947 Hz	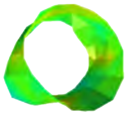	3052 Hz	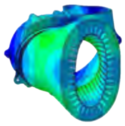	3.6%
3,0	4584 Hz	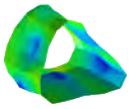	4758 Hz	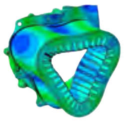	3.8%

Each hammer test is repeated five times and the output frequency response functions (FRFs) are obtained by averaging the different tests. This process is automatically managed by the software Simcenter Testlab 2406 [44]. To simulate numerically the hammer test, as shown in Figure 11b, a unit radial load is introduced at the same point as the experimental test and the resulting accelerations are compared to the experimentally measured ones.

The FRFs, obtained from the hammer test, whose input and output are depicted in Figure 11b, is shown and compared to the numerical one in Figure 11a. The numerical results align closely with the experimental data, confirming that the structural dynamics are well captured. Peaks at approximately 2000 Hz, 3000 Hz and 4500 Hz are clearly visible in both cases, validating the mode identification.

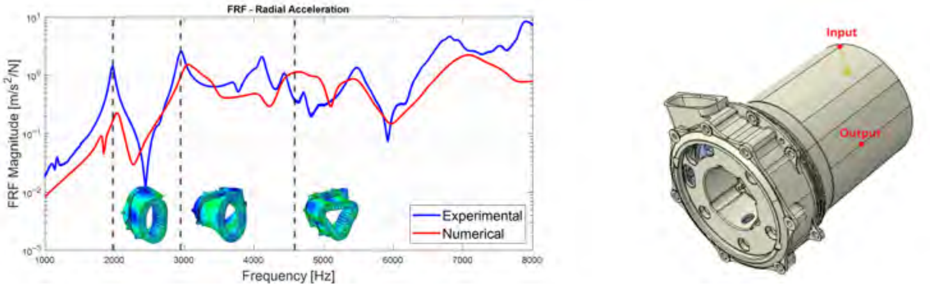

(**a**) (**b**)

Figure 11. FRFs of the hammer test with the Jacket model. (**a**) Numerical/Experimental FRFs. (**b**) Input output position.

5.1. Effect of the Cooling Fluid

The second model, shown in Figure 12, represents the full motor mounted on the test bench, with fixed boundary conditions applied at the mounting points. This Complete model was used for modal, frequency response and forced vibration analyses under both drag and full-load conditions.

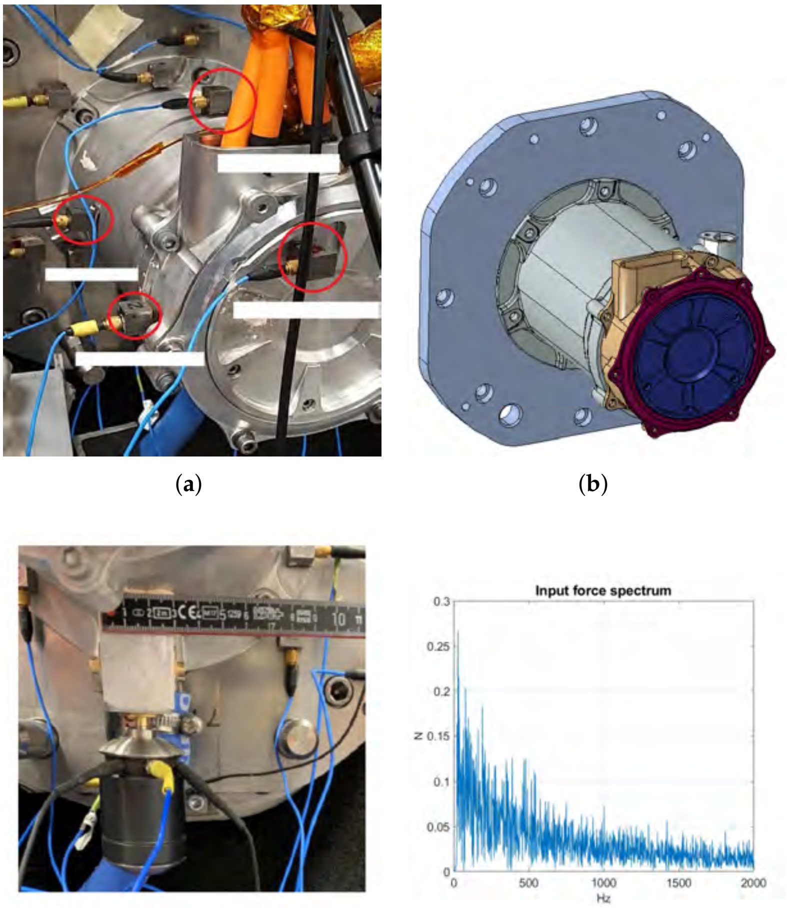

(**a**) (**b**)

(**c**) (**d**)

Figure 12. Complete model. (**a**) Experimental setup with highlighted accelerometers. (**b**) Numerical model. (**c**) Shaker. (**d**) Shaker force profile.

To validate the numerical model and evaluate the effect of the cooling fluid, a forced response experiment was performed on the physical prototype using a Q-ISH inertia shaker. As shown in Figure 12c, the shaker was directly bonded to the housing. It vibrates, generating a defined input force spectrum into the system. The output vibration on the housing is measured by means of the accelerometers encircled in Figure 12a. The measured accelerations are then used to estimate the frequency response function. The force spectrum applied to the prototype PMSM is depicted in Figure 12d. Due to the limitations of the shaker test rig, the experimental measurements were conducted up to 2 kHz, allowing only the first bending mode to be clearly identified. For this reason, the numerical simulations were limited to the same frequency range to ensure a consistent and meaningful comparison.

The numerical simulation predicted the first bending mode at 338 Hz, demonstrating excellent correlation and validating the reliability of the model for NVH analyses.

While the cooling fluid is included in the experimental setup, its representation is often neglected in numerical simulations due to modeling complexity and increased computational demands. To quantify its effect, two versions of the Complete model were simulated: one with the cooling fluid and one without. The resulting FRFs, shown in Figure 13, reveal a significant difference. Moreover, the inclusion of the fluid domain in the FEM model leads to the presence of new natural modes at lower frequencies, which do not appear when the fluid is neglected. While the simulation without cooling fluid captures the general trend, it fails to match the resonance peaks and dynamic response. Conversely, the simulation including the fluid exhibits excellent agreement with the experimental results, both in terms of amplitude and frequency content, within the 0–2 kHz range.

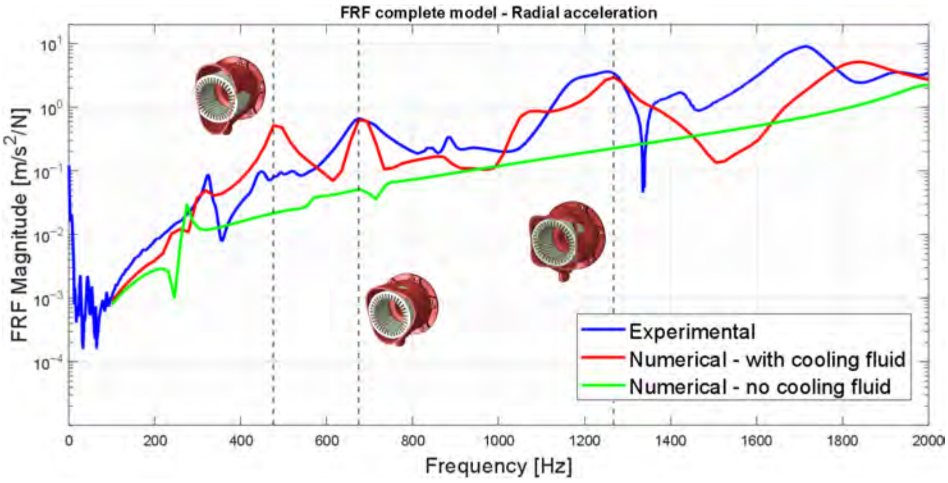

Figure 13. FRFs from the shaker test and numerical simulations, comparing results with and without cooling fluid in the Complete model.

A clear example is mode 2, which appears at 476 Hz when the cooling fluid is modeled, whereas in the simulation without fluid the closest comparable mode is found at 1997 Hz. This significant difference indicates the appearance of a distinct vibration mode resulting from the fluid–structure interaction, consistently with the findings of [36]. The cooling fluid enables vibrational energy transfer between the stator and the housing, thereby substantially altering the overall dynamic behavior of the system. The main peaks up to 2000 Hz are associated with the eigenmodes of the housing, as illustrated in Figure 13, whereas the modes of the laminated stator do not contribute in this frequency range because their natural frequencies are significantly higher. This is confirmed by Table 9, which reports the main numerical structural modes and clearly shows that the stator modes are all located above 2000 Hz.

5.2. Forced Vibration Analysis

A high correlation of the structural numerical model is essential to produce accurate results in NVH analyses. Once validated, the model can be used to perform forced vibration simulations under both drag and full-load conditions, by applying the electromagnetic forces obtained from electromagnetic simulations.

To define the electromagnetic loads in the structural model, a nodal transfer force method has been implemented. This approach consists of replicating the same mesh layout at the tooth head interface in both the electromagnetic and structural models, allowing for a direct node-to-node mapping of the forces. In this way, the electromagnetic distributions were spatially projected onto the structural mesh, ensuring the consistency of the excitation profile.

Table 9. Numerical natural frequencies f_n and corresponding mode shapes of the Complete model.

Mode	Natural Frequency f_n	Mode Shape
0	9239 Hz	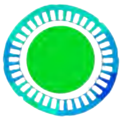
2	2027 Hz	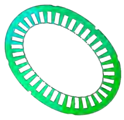
3	4595 Hz	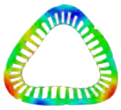
4	7355 Hz	

Electromagnetic simulations were performed using Flux 2D 2022, with the resulting data exported and post-processed in MATLAB 2022b. This post-processing included transforming the time-domain results into the frequency domain, isolating the dominant electromagnetic orders, and mapping the forces to the appropriate structural nodes. The data were then imported into Abaqus CAE, where harmonic analyses were performed considering only mechanical time orders 6 and 36. This choice is motivated by the following considerations. The sixth order corresponds to the highest electromagnetic force component, as shown in Figure 3. The 36th order has been found to dominate the dynamic response of the structure, according to the analytical model results. This order excites a breathing-type deformation of the stator, which is particularly relevant in NVH, as it efficiently radiates acoustic energy through the housing. Such modes are often responsible for tonal noise and are critical targets in acoustic optimization [14]. The electromagnetic forces were validated by computing the torque from the tangential components and confirming that it matched the torque measured at the test bench.

The structural response of the Complete model in drag conditions are reported in Figure 14. As shown in Figure 14a, the stator exhibits a six-lobed shape, which reflects the main spatial distribution of the sixth-order electromagnetic forces. For this order, the most significant peak occurs at 2000 Hz, where the housing also assumes a six-lobed deformation pattern. In contrast, for the 36th time order, the most prominent peak appears at 8986 Hz and corresponds to the excitation of the breathing mode. In this case, the stator does not exhibit any lobed shape, which is consistent with the characteristics of the excitation forces. The housing-related modes (i.e., two-lobed, three-lobed, and four-lobed patterns), previously identified in the FRF analysis (Figure 13), were also observed during the transient ramp simulation.

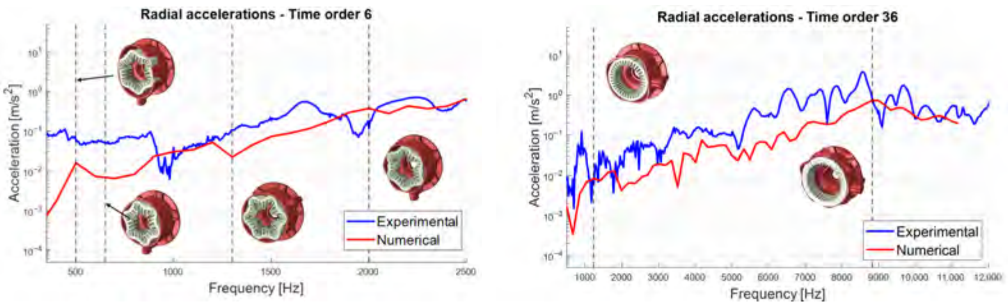

(**a**) (**b**)

Figure 14. Radial acceleration profiles in drag condition. (**a**) Time order 6. (**b**) Time order 36.

The structural response of the Complete model under full-load conditions, within the constant torque speed range, is shown in Figure 15. In this case, furthermore, a close agreement between the experimental and numerical results is observed. Compared to the drag condition, the full-load condition exhibits a similar trend, but with higher acceleration levels. This increase is attributed to the larger amplitude of the electromagnetic force components.

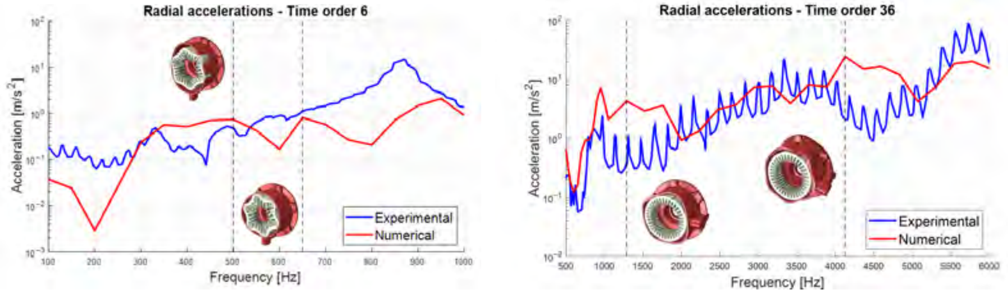

(**a**) (**b**)

Figure 15. Radial acceleration profiles in full-load condition. (**a**) Time order 6. (**b**) Time order 36.

6. Numerical Acoustic Model

The final stage of the numerical analysis involves simulating the acoustic emission resulting from the vibrations of the motor. To reduce the computational cost, a separate acoustic-only model is developed. The acoustic domain is modeled as a hollow cylinder, where the internal surface corresponds to the negative volume of the structural assembly. A non-reflecting boundary condition is applied to the external surface of the acoustic domain, allowing sound pressure waves to propagate through the boundary without reflections. The minimum stand-off distance r_1, representing the radial gap between the outer surface of the motor and the outer boundary of the acoustic domain, is computed as

$$r_1 \geq \frac{c \cdot n_{min}}{f_{min}} \tag{8}$$

where c is the speed of sound in air, $n_{min} = \frac{1}{3}$ is the number of wavelengths between the source and the boundary, and f_{min} is the minimum frequency of interest [5]. The acoustic medium is defined by a density of $1.293\,\mathrm{kg/m^3}$ and a bulk modulus of $142\,\mathrm{MPa}$. The acoustic mesh consists of the following:

- Two-dimensional ASI3D3 linear triangular elements, defining the acoustic interface and representing the internal surfaces of the motor (i.e., the structural-acoustic coupling surface).

- Three-dimensional AC3D4 linear tetrahedral elements, used to discretize the volume of the acoustic domain.

  The mesh element size plays a key role in result accuracy and is constrained by

$$L_{max} < \frac{c}{m_{min} f_{max}} \tag{9}$$

where $m_{min} = 6$ is the number of inter-nodal intervals per wavelength and f_{max} is the maximum frequency of interest [5]. This yields a maximum element size of 23 mm for time integration order 6, and 4 mm for order 36.

The output of the simulation is the pressure distribution within the acoustic domain. A virtual microphone is placed in the same position as in the experimental setup (50 mm from housing surface) to allow comparison between simulated and measured data. Structural excitation is applied via boundary submodel conditions, with displacement imposed at the acoustic interface.

The acoustic emission of the Complete model in drag conditions are reported in Figure 16. Overall, the numerical model provides results that are in good agreement with the experimental measurements, demonstrating its high level of accuracy. Consistent with the results of the vibration analysis, the most prominent peak in the sixth time order appears in the higher frequency range and corresponds to the excitation of the six-lobed mode of the housing. In the 36th time order, the dominant peak occurs at 9320 Hz and is associated with the excitation of the breathing mode.

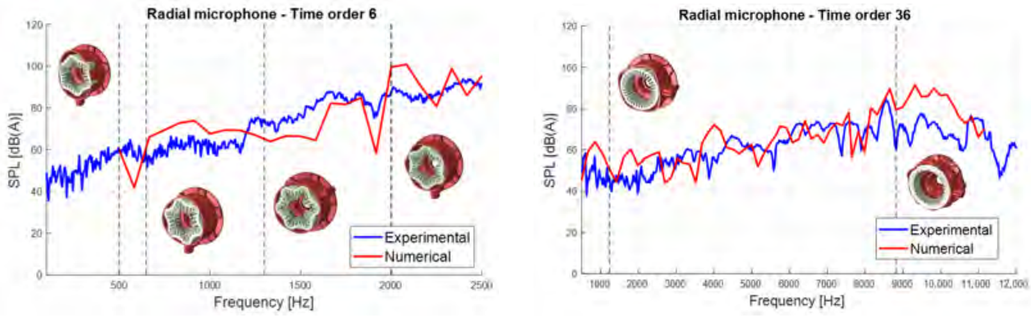

(**a**) (**b**)

Figure 16. SPL profiles in drag condition. (**a**) Time order 6. (**b**) Time order 36.

The acoustic response of the Complete model in full-load conditions are reported in Figure 17, governed by the breathing mode. In general, it can be observed that the acoustic emission prediction is more accurate in drag conditions than in full-load conditions.

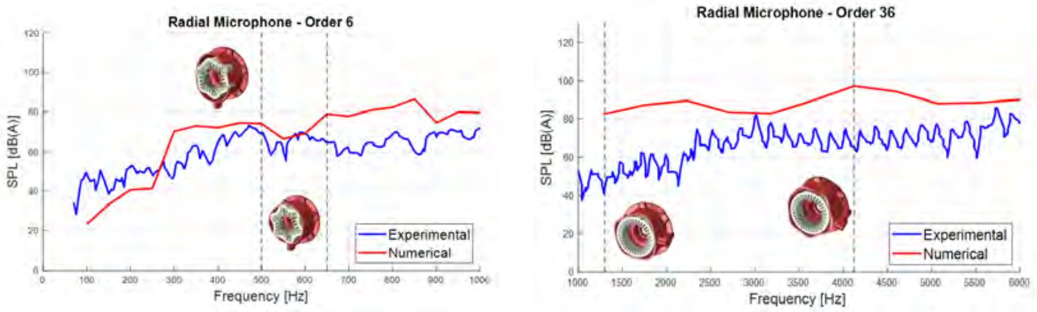

(**a**) (**b**)

Figure 17. SPL profiles in full-load condition. (**a**) Time order 6. (**b**) Time order 36.

7. Conclusions

This study describes a novel and effective method for predicting the NVH behavior of a 6–36 pole–slot PMSM with distributed hairpin winding, combining homogenized material properties, coupled fluid–structure interaction and integrated analytical and numerical modeling applied to a real-world automotive electric motor. Radial and tangential electromagnetic forces were calculated using finite element analysis under both drag and full-load conditions. The 6th and 36th time orders emerged as dominant. The former is primarily associated with a six-lobed spatial mode, while the latter corresponds to a zero-order breathing mode. Two structural models were developed and presented: an analytical model and a numerical model. The analytical model is capable of predicting acoustic emission with a reduced computational cost. It highlighted that spatial radial forces of order 0 are particularly critical for this motor, as they excite the breathing mode in the resonance region during operating conditions. These results were confirmed by a high-fidelity numerical model, albeit with a significantly higher computational cost. The FE model adopted is based on a physical derivation of the mechanical properties of the laminated stator and windings, without requiring experimental corrections or tuning. This represents a significant advantage in predictive NVH assessment. Its accuracy was validated by comparing numerical and experimental modal analysis and FRFs.

The importance of accurately including the cooling fluid in the NVH model was demonstrated. The coolant introduces fluid–structure interaction within the motor, which is essential to capture the main deformation modes. Without accounting for the coolant, the numerical model fails to capture the relevant dynamic behavior, leading to the potentially incorrect identification of resonant frequencies. The vibration results obtained by this modeling approach closely matched experimental measurements, confirming the accuracy of the approach. Hence, incorporating the coolant represents a methodological improvement that enhances NVH-oriented design compared to traditional models that neglect fluid effects.

The acoustic emission of the motor was evaluated numerically. The acoustic domain was modeled using the finite element method, with appropriate boundary conditions applied. Near-field measurements were carried out under both drag and full-load conditions, showing high correlation with numerical predictions.

This integrated, multiphysics, multi-domain approach provides a solid foundation for NVH prediction in electric motor development, bridging early-stage design with high-fidelity simulations and enabling efficient, simulation-driven design iterations. Moreover, the structure of the proposed modeling approach is modular, allowing easy adaptation to different PMSM geometries, materials, and cooling topologies. This ensures the versatility and reusability of the approach across a wide range of motor designs.

Future work will focus on the experimental validation of electromagnetic excitation forces, in order to confirm the accuracy of the electromagnetic numerical models.

Author Contributions: Conceptualization, D.B., F.S., F.M.B. and M.G.; methodology, P.A., D.B., F.S., G.G., M.G. and F.M.B.; validation, P.A., D.B. and F.S.; formal analysis, D.B., F.S. and F.M.B.; investigation, P.A. and G.G.; resources, M.G.; data curation, P.A., D.B. and F.S.; writing—original draft preparation, P.A., D.B. and F.S.; writing—review and editing, G.G., F.M.B. and M.G.; visualization, P.A., D.B., G.G. and F.S.; supervision, F.M.B. and M.G.; project administration, M.G. All authors have read and agreed to the published version of the manuscript.

Funding: This research received no external funding.

Data Availability Statement: The original contributions presented in the study are included in the article; further inquiries can be directed to the corresponding author.

Conflicts of Interest: The authors declare no conflicts of interest.

References

1. Guidotti, G.; Barri, D.; Soresini, F.; Gobbi, M. Optimal Design of Interior Permanent Magnet Synchronous Motor Considering Various Sources of Uncertainty. *World Electr. Veh. J.* **2025**, *16*, 79. [CrossRef]
2. Pindoriya, R.M.; Rajpurohit, B.S.; Kumar, R. A Novel Application of Harmonics Spread Spectrum Technique for Acoustic Noise and Vibration Reduction of PMSM Drive. *IEEE Access* **2020**, *8*, 103273–103284. [CrossRef]
3. Horváth, K.; Zelei, A. Simulating Noise, Vibration, and Harshness Advances in Electric Vehicle Powertrains: Strategies and Challenges. *World Electr. Veh. J.* **2024**, *15*, 367. [CrossRef]
4. Gonzalez, P.; Buigues, G.; Mazon, A.J. Noise in Electric Motors: A Comprehensive Review. *Energies* **2023**, *16*, 5311. [CrossRef]
5. Soresini, F.; Barri, D.; Ballo, F.; Gobbi, M.; Mastinu, G. Noise and Vibration Modeling of Permanent Magnet Synchronous Motors: A Review. *IEEE Trans. Transp. Electrif.* **2024**, *10*, 8728–8745. [CrossRef]
6. Remus, N.; Toulabi, M.S.; Mukundan, S.; Dhulipati, H.; Li, W.; Novak, C.; Kar, N.C. Electromagnetic Noise and Vibration in PMSM and Their Sources: An Overview. In *Proceedings of the 2020 IEEE Canadian Conference on Electrical and Computer Engineering (CCECE)*; IEEE: Piscataway, NJ, USA, 2020; pp. 1–4. [CrossRef]
7. Gieras, J.F.; Wang, C.; Lai, J.C. *Noise of Polyphase Electric Motors*; CRC Press: Boca Raton, FL, USA, 2018.
8. Pile, R.; devillers, E.; Le Besnerais, J. Comparison of Main Magnetic Force Computation Methods for Noise and Vibration Assessment in Electrical Machines. *IEEE Trans. Magn.* **2018**, *54*, 8104013. [CrossRef]
9. Lin, F.; Zuo, S.; Wu, X. Electromagnetic vibration and noise analysis of permanent magnet synchronous motor with different slot-pole combinations. *IET Electr. Power Appl.* **2016**, *10*, 900–908. [CrossRef]
10. Soresini, F.; Barri, D.; Manzoni, S.; Ballo, F.; Gobbi, M. Modal characterization of a PMSM using different experimental techniques. In *Proceedings of the ISMA 2024—International Conference on Noise and Vibration Engineering and USD 2024—International Conference on Uncertainty in Structural Dynamics*; KU Leuven, Departement Werktuigkunde: Leuven, Belgium, 2024; pp. 2852–2865.
11. Yang, H.; Chen, Y. Influence of Radial Force Harmonics with Low Mode Number on Electromagnetic Vibration of PMSM. *IEEE Trans. Energy Convers.* **2014**, *29*, 38–45. [CrossRef]
12. Islam, M.S.; Islam, R.; Sebastian, T. Noise and Vibration Characteristics of Permanent-Magnet Synchronous Motors Using Electromagnetic and Structural Analyses. *IEEE Trans. Ind. Appl.* **2014**, *50*, 3214–3222. [CrossRef]
13. Xu, Y.; Xu, Z.; Zou, J.; Yu, G. Zeroth-Mode Vibration Suppression for Integral-Slot Surface-Mounted PMSMs by Increasing the Vibration Mode From Zero to Number of Pole Pair. *IEEE Trans. Transp. Electrif.* **2025**, *11*, 2829–2839. [CrossRef]
14. Hofmann, A.; Qi, F.; Lange, T.; De Doncker, R.W. The breathing mode-shape 0: Is it the main acoustic issue in the PMSMs of today's electric vehicles? In *Proceedings of the 2014 17th International Conference on Electrical Machines and Systems (ICEMS)*; IEEE: Piscataway, NJ, USA, 2014; pp. 3067–3073. [CrossRef]
15. Deng, W.; Zuo, S. Electromagnetic Vibration and Noise of the Permanent-Magnet Synchronous Motors for Electric Vehicles: An Overview. *IEEE Trans. Transp. Electrif.* **2019**, *5*, 59–70. [CrossRef]
16. Mendizabal, M.; McCloskey, A.; Poza, J.; Zarate, S.; Iriondo, J.; Irazu, L. Optimum Slot and Pole Design for Vibration Reduction in Permanent Magnet Synchronous Motors. *Appl. Sci.* **2021**, *11*, 4849. [CrossRef]
17. Chai, F.; Li, Y.; Pei, Y.; Li, Z. Accurate modelling and modal analysis of stator system in permanent magnet synchronous motor with concentrated winding for vibration prediction. *IET Electr. Power Appl.* **2018**, *12*, 1225–1232. [CrossRef]
18. McCloskey, A.; Arrasate, X.; Hernández, X.; Gómez, I.; Almandoz, G. Analytical calculation of vibrations of electromagnetic origin in electrical machines. *Mech. Syst. Signal Process.* **2018**, *98*, 557–569. [CrossRef]
19. Zhang, B.; Zhao, T.; Yang, M.; Wang, Q.; Cui, S. Analytical Calculation Method of Motor Natural Frequencies Based on Equivalent Model of Three-Layer Cylindrical Shell. *IEEE Trans. Ind. Electron.* **2022**, *70*, 6078–6089. [CrossRef]
20. Yin, H.; Zhang, X.; Ma, F.; Gu, C.; Gao, H.; Wang, Y. New equivalent model and modal analysis of stator core-winding system of permanent magnet motor with concentrated winding. *IEEE Access* **2020**, *8*, 78140–78150. [CrossRef]
21. Hou, P.; Ge, B.; Tao, D.; Wang, Y.; Pan, B. Coupling analysis of electromagnetic vibration and noise of FeCo-based permanent-magnet synchronous motor. *Energies* **2022**, *15*, 3888. [CrossRef]
22. Park, S.; Kim, W.; Kim, S.I. A numerical prediction model for vibration and noise of axial flux motors. *IEEE Trans. Ind. Electron.* **2014**, *61*, 5757–5762. [CrossRef]
23. Millithaler, P.; Sadoulet-Reboul, É.; Ouisse, M.; Dupont, J.B.; Bouhaddi, N. Structural dynamics of electric machine stators: Modelling guidelines and identification of three-dimensional equivalent material properties for multi-layered orthotropic laminates. *J. Sound Vib.* **2015**, *348*, 185–205. [CrossRef]
24. Kim, J.H.; Park, S.H.; Ryu, J.Y.; Lim, M.S. Comparative Study of Vibration on 10-Pole 12-Slot and 14-Pole 12-Slot PMSM Considering Tooth Modulation Effect. *IEEE Trans. Ind. Electron.* **2023**, *70*, 4007–4017. [CrossRef]
25. Deng, W.; Dong, C.; Qian, Z.; Wang, Q. Equivalent orthotropic material parameters identification of electrical machines for modal analysis utilizing a PSO-assisted theoretical approach. *Mech. Syst. Signal Process.* **2025**, *222*, 111765. [CrossRef]

26. Marcon, J.C.; Silva, O.M.; Fiorentin, T.A.; Lenzi, A. Identification of Three-Dimensional Equivalent Material Properties for Laminated Disks Pack of Electric Machine Stators: Application in Reciprocal Compressors. *Shock Vib.* **2019**, *2019*, 9029026. [CrossRef]
27. Ciceo, S.; Chauvicourt, F.; Gyselinck, J.; Martis, C. Data-driven electrical machines structural model using the vibration synthesis method. *IEEE Trans. Transp. Electrif.* **2022**, *8*, 3771–3781. [CrossRef]
28. Zhang, Z.; Jiao, Z.; Xia, H.; Yao, Y. Parameter Equivalent Method of Stator Anisotropic Material Based on Modal Analysis. *Energies* **2019**, *12*, 4257. [CrossRef]
29. Yin, H.; Ma, F.; Zhang, X.; Gu, C.; Gao, H.; Wang, Y. Research on Equivalent Material Properties and Modal Analysis Method of Stator System of Permanent Magnet Motor with Concentrated Winding. *IEEE Access* **2019**, *7*, 64592–64602. [CrossRef]
30. Sun, R.; Ma, C.; Hou, Q.; Chen, D. Accurate modal analysis method for automotive drive motors considering composite structures and impregnating windings in the design phase. *IEEE Trans. Transp. Electrif.* **2024**, *10*, 9931–9944. [CrossRef]
31. Saki, A.; Kiyoumarsi, A.; Ariaei, A. An equivalent and simplified approach for acoustic noise prediction in a PM synchronous motor based on the semi-analytical-FEM model. *IET Electr. Power Appl.* **2024**, *18*, 1200–1213. [CrossRef]
32. Wang, Y.; Gao, H.; Wang, H.; Ma, W. NVH Optimization Analysis of Permanent Magnet Synchronous Motor by Rotor Slotting. *Vehicles* **2020**, *2*, 287–302. [CrossRef]
33. Song, P.; Li, W.; Mukundan, S.; Kar, N.C. An overview of noise-vibration-harshness analysis for induction machines and permanent magnet synchronous machines. In *Proceedings of the 2020 10th International Electric Drives Production Conference (EDPC)*; IEEE: Piscataway, NJ, USA, 2020; pp. 1–8.
34. Zhang, H.; Jaura, A.; Kumar, D.; Sambharam, T.; Zhang, Z.; He, S.; Zhang, P.; GSJ, G. Multiphysics Simulation of Electric Motor NVH Performance with Eccentricity. In *Proceedings of the Noise and Vibration Conference & Exhibition*; SAE International: Warrendale, PA, USA, 2021. [CrossRef]
35. Zhao, S.; Chen, J.; Zhang, C.; Gao, Y. Vibration Prediction Based on Hybrid Model of Surface-Mounted PMSM Considering Different Topologies and Tooth Modulation. *IEEE Trans. Ind. Appl.* **2025**, *61*, 6172–6182. [CrossRef]
36. Barri, D.; Soresini, F.; Ballo, F.; Lucà, F.; Manzoni, S.; Gobbi, M.; Mastinu, G. NVH Performance of Permanent Magnet Synchronous Motors with Liquid Cooling System. *SAE Int. J. Veh. Dyn. Stab. NVH* **2025**, *9*, 69–84. [CrossRef]
37. Schnell, M.; Gauterin, F. Acoustic effects of the coolant mass flow of an electric machine of a hybrid drive train. *Automot. Engine Technol.* **2019**, *4*, 189–193. [CrossRef]
38. Ballo, F.; Gobbi, M.; Mastinu, G.; Palazzetti, R. Noise and vibration of permanent magnet synchronous electric motors: A simplified analytical model. *IEEE Trans. Transp. Electrif.* **2022**, *9*, 2486–2496. [CrossRef]
39. Rao, S.S. *Vibration of Continuous Systems*; John Wiley & Sons: Hoboken, NJ, USA, 2019.
40. Urreta, S.; Salva, H.; Ghilarducci, A.; Billoni, O.; Fabietti, L. Elasticity in nanocrystalline Nd2Fe14B+ αFe magnetic composites. *Phys. B Condens. Matter* **2002**, *320*, 297–299. [CrossRef]
41. Ansys Inc. *Ansys Material Designer*; Ansys Inc.: Canonsburg, PA, USA, 2024.
42. Orban, F. Damping of materials and members in structures. *Proc. J. Phys. Conf. Ser.* **2011**, *268*, 012022. [CrossRef]
43. Peeters, B.; Van der Auweraer, H. PolyMAX: A revolution in operational modal analysis. In Proceedings of the 1st International Operational Modal Analysis Conference, Copenhagen, Denmark, 26–27 April 2005; Volume 820, pp. 1–12.
44. Siemens Digital Industries Software. *Simcenter Testlab 2406*; Siemens Digital Industries Software: Plano, TX, USA, 2024.